Applied Physics A (2020) 126:73
https://doi.org/10.1007/s00339-019-3260-y

Applied Physics A
Materials Science & Processing

Analysis of varying Gd^{3+} concentrations on the structure and optical properties of $ZnAl_2O_4$:0.1% Eu^{3+}; *x*% Gd^{3+} ($0 \le x \le 1.2$) synthesized via citrate sol–gel method

V. M. Maphiri[1] · Y. Dwivedi[2] · L. F. Koao[3] · R. E. Kroon[4] · S. V. Motloung[1,5]

Received: 7 November 2019 / Accepted: 22 December 2019 / Published online: 2 January 2020

Abstract
We report the preparation of 0.1% Eu^{3+}; *x*% Gd^{3+} ($0 \le x \le 1.2$) $ZnAl_2O_4$ phosphors using the citrate sol–gel method. X-ray diffraction (XRD) data revealed that all annealed samples consisted of the single phase of cubic $ZnAl_2O_4$ structure. The scanning electron microscopic (SEM) images indicated pronounced effect of dual doping on the surface morphology of the phosphor. The estimated crystal sizes estimated by the XRD was confirmed by the high-resolution transmission electron microscopy (HR-TEM) to be approximately around 20 nm. The photoluminescence (PL) spectroscopy results revealed four distinct emission peaks located at 393, 400, 578 and 618 nm. The peaks at around 393 and 400 nm were attributed to the defect levels located at different positions on the host material ($ZnAl_2O_4$). The emission peak at 578 and 618 nm were attributed to the $^5D_0 \rightarrow {}^7F_1$ and $^2D_0 \rightarrow {}^7F_2$ characteristic transition within the Eu^{3+} ions. The International Commission on Illumination (CIE) colour coordinates revealed that the emission colour was not influenced by varying the concentration of Gd^{3+}.

Keywords Citrate sol–gel · Photoluminescence · $ZnAl_2O_4$ · Eu · Gd co-doped · CIE

1 Introduction

Zinc aluminate ($ZnAl_2O_4$) is one of the representative compounds in the family of metal aluminate, with the spinel structure, and it is widely used as ceramic, electronic, catalytic material, etc. [1]. $ZnAl_2O_4$ also possesses a remarkable combination of properties such as high thermal, chemical stability, better ductility, low surface acidity, moderate conductivity and high quantum yields [1-3]. $ZnAl_2O_4$ is a wide band gap semiconductor with an optical band gap of ~ 3.8 eV, which makes it useful for photo-electronic devices [2]. Recently, researchers have also shown that $ZnAl_2O_4$ phosphor has many applications in stress imaging devices, thin film electroluminescent displays and mechano-optical stress sensors [2, 3]. $ZnAl_2O_4$ is known to crystalize under the normal spinel structural configuration with the chemical formula AB_2O_4, where A represents the divalent cation (Zn^{2+}) that occupies the tetrahedral sites and B represents the trivalent cation (Al^{3+}) that occupies the octahedral sites of a close packed crystal structure that belongs to the space group Fd3m. The unit cell contains 32 oxygen (O^{2-}) anions, 16 Al^{3+} cations and 8 Zn^{2+} cations [4]. The literature has shown that $ZnAl_2O_4$ can be synthesized by numerous types of wet chemical techniques [5, 6], e.g. to fabricate $ZnAl_2O_4$ doped with rare earth (RE) metals [6]. Strek et al. [7] prepared $ZnAl_2O_4$:Eu^{3+} via the hydrothermal method and used X-ray diffraction (XRD) to demonstrate the formation of a single phase of $ZnAl_2O_4$ nanopowders with high crystallinity. The size of the nanocrystallites was determined to be 8 and 15 nm for samples heated at 500 and 1000 °C, respectively. However, details of the synthesis

✉ V. M. Maphiri
vusanimuswamaphiri@gmail.com

✉ S. V. Motloung
cchataa@gmail.com

1 Department of Physics, Sefako Makgatho Health Science University, PO Box 94, Medunsa 0204, South Africa

2 Department of Physics, National Institute of Technology Kurukshetra, Kurukshetra, Haryana 136119, India

3 Department of Physics, University of the Free State (Qwaqwa Campus), Private Bag X13, Phuthaditjhaba 9866, South Africa

4 Department of Physics, University of the Free State, PO Box 339, Bloemfontein 9300, South Africa

5 Department of Physics, Nelson Mandela University, PO Box 77000, Port Elizabeth 6031, South Africa

and spectroscopic characterization of Gd-doped $ZnAl_2O_4$ nanophosphor were not located in open resources. Gd^{3+} has been reported as part of the host [8] and as a dopant of Y_2O_3 [9]. Zatsepin et al. [8] studied the intrinsic luminescence of Gd_2O_3. They reported that the cubic polymorph exhibited an intrinsic luminescence due to "defective" Gd^{3+} ions at 315 nm. This ultraviolet emission is the consequence of 232 and 275 nm 4–4f excitation. Tamrakar et al. [9] investigated the emission of cubic Y_2O_3:Gd^{3+}. The photoluminescence (PL) spectra suggested the presence of three distinct emission peaks located at 314, 317 and 395 nm. These peaks were due to the transitions between excited states ^6I_j, ^6P_j to the ground energy level $^8S_{7/2}$ of Gd^{3+} ions. Eu^{3+} has previously been reported as a dopant in $ZnAl_2O_4$ [10] and other host materials [11]. Motloung et al. [10] studied the $ZnAl_2O_4$:0.1% Ce^{3+};x% Eu^{3+} dual-doped system and the PL results showed emission peaks that were attributed to the host defects and Ce^{3+} and Eu^{3+} transitions, as well as confirming energy transfer (ET) from $Ce^{3+} \rightarrow Eu^{3+}$. On the contrary, Chengaiah et al. [11] showed the existence of energy transfer from $Eu^{3+} \rightarrow Ce^{3+}$ in $Na_3Gd(PO_4)_2$:Eu^{3+}; Ce^{3+} co-doped phosphor. Thus, the ET pathways or direction can be controlled to either favour $Ce^{3+} \rightarrow Eu^{3+}$ or $Eu^{3+} \rightarrow Ce^{3+}$.

From an in-depth literature review, it is clear that there are many investigations on the doping of $ZnAl_2O_4$ with different ions [5-7, 10]. However, there is no reported investigation exploring the $ZnAl_2O_4$ nano-sized host co-doped with Eu^{3+} and Gd^{3+} ions. The present report is based on an investigation pertaining to the effect of varying the Gd^{3+} concentration on the structure and optical properties of $ZnAl_2O_4$:0.1% Eu^{3+}; x% Gd^{3+} co-doped phosphor material synthesized by the citrate sol–gel process. The primary objective of the current work is to develop alternative phosphor materials for practical applications such as for light emitting diodes (LEDs). The photophysics related to the excitation and de-excitation processes is explained in detail.

2 Experimental procedure

2.1 Samples synthesis

$ZnAl_2O_4$ (host), singly doped (with 0.1% Eu^{3+} or 0.1% Gd^{3+}) and co-doped with 0.1% Eu^{3+}; x% Gd^{3+} ($0 \leq x \leq 1.2$), nanophosphors were synthesized using the citrate sol–gel technique. The host (undoped) material was prepared by dissolving $Zn(NO_3)_2{\cdot}6H_2O$ (98%), $Al(NO_3)_3{\cdot}9H_2O$ (98.5%) and citric acid (CA) $C_8H_8O_7{\cdot}H_2O$ (99%) in deionized water. The stoichiometric molar ratio of Zn:Al and Zn:CA was kept at 1:2 and 1:0.75, respectively. Specified amounts of $Gd(NO_3)_3{\cdot}6H_2O$ (99.9%) and $Eu(NO_3)_3{\cdot}5H_2O$ (99.9%) were added into separate beakers to singly dope with 0.1% Eu^{3+} and 0.1% Gd^{3+}. All chemicals were purchased from Sigma-Aldrich. The co-doped samples were prepared by keeping the 0.1% Eu^{3+} concentration constant and varying the x% Gd^{3+} concentration over a range $0 \leq x \leq 1.2$. The heating temperature was kept at ~80 °C while constantly stirring using a magnetic stirrer until gels were formed. These were subsequently annealed in air at 800 °C in a furnace for 1 h. The products were crushed using a pestle and mortar to produce powders.

2.2 Characterization

The crushed powder samples were then analysed using different techniques. The crystal structure and phase composition of the prepared powder samples were analysed with a Bruker D8-Advance powder with a CuKα (1.5405 Å) radiation. The prepared powder was carbon coated using the Quorum carbon coater and the Tescan VEGA3 scanning electron microscope (SEM) coupled with Oxford XMax^N energy-dispersive X-ray spectroscope (EDS) was used to study the surface morphology and elementary composition. Transmission electron microscopy (TEM) was performed with a JEOL JEM 1010 to study the size and shape of powder samples. Photoluminescence (PL) spectra measurements were performed at room temperature by the Hitachi F-7000 fluorescence spectrophotometer using xenon lamp as an excitation source and the lifetime measurements were taken at the chopping speed of 20 Hz.

3 Results and discussion

3.1 XRD analysis

The XRD patterns of the prepared samples are shown in Fig. 1. The prepared samples are polycrystalline with a structure that matches the standard pattern of cubic $ZnAl_2O_4$ spinel (JCPDS 82-1043). This crystalline structure was expected to alter in the presence of RE ions due to the comparably larger size of the dopants at substitutional sites, but due to the low concentration of the dopants the structure was found to remain the same. Additional diffraction peaks were not observed, suggesting no Eu^{3+}- and/or Gd^{3+}-related impurities and indicating a successful substitution of either Zn^{2+} or Al^{3+} by the Eu^{3+} and/or Gd^{3+} ions within the host lattice. Thus, the presence of symmetric and strong diffraction peaks indicates the growth of monophase $ZnAl_2O_4$ crystallites at an annealing temperature of 800 ºC.

The analysis of the 311 diffraction peaks for the prepared samples is presented in Fig. 2. It is noted that the incorporation of foreign atoms into the host matrix influences the diffraction intensity and peak angle. The decrease or increase of the diffraction intensity in Fig. 2 can be attributed to the loss or gain of crystalline quality [12]. When comparing the

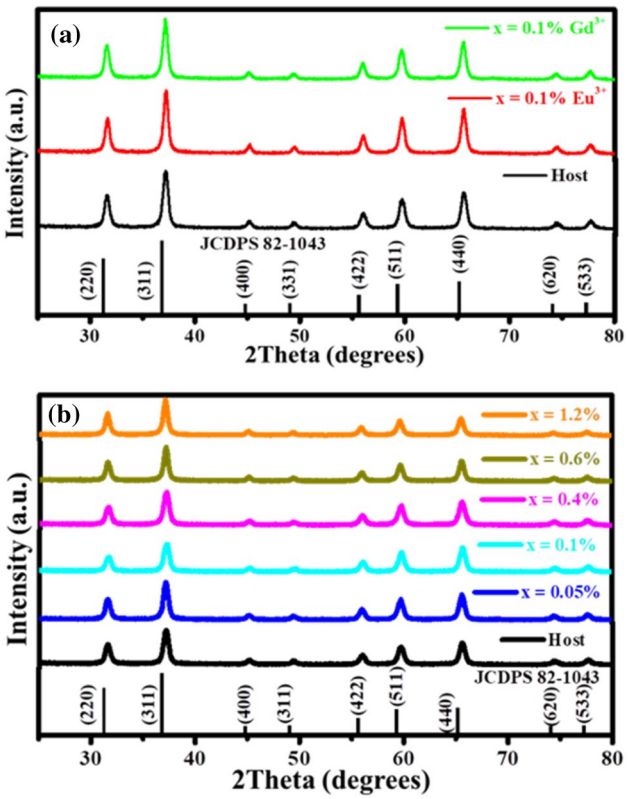

Fig. 1 The XRD patterns for the **a** host, singly doped (with 0.1% Eu^{3+} and 0.1% Gd^{3+}) and **b** $ZnAl_2O_4$:0.1% Eu^{3+}; x% Gd^{3+} ($0 \le x \le 1.2$) co-doped samples

peak diffraction angle of the host and singly doped samples in Fig. 2a, there is a slight peak shift to higher diffraction angle, which indicates a slight decrease in the lattice parameters. The ionic radius of both Zn^{2+} (0.74 Å) and Al^{3+} (0.53 Å) [7] is smaller than that of Eu^{3+} (0.95 Å) [13] and Gd^{3+} (1.08 Å) [3]. It is predicted by Vegard's law [14, 15] that if the incorporation process takes place via substitution, the addition of Eu^{3+} and/or Gd^{3+} should expand the lattice. Figure 2a shows a clear indication of the violation of Vegard's law. Similar results have been previous observed in the $ZnAl_2O_4$:Pb^{2+} system [16], where at lower Pb^{2+} concentration the lattice parameter decreased. This behaviour was attributed to the shrinkage of the Pb^{2+} outer electron shell due to its electronic interactions with neighbouring Zn^{2+} ions. Figure 2b shows the variation in diffraction angle of the co-doped sample when varying the concentration of Gd^{3+} ion ($0 \le x \le 1.2$). The peaks seem to shift to a lower diffraction angle indicating an increase in the lattice angle, expect for $x = 0.1\%$, and the reason for this behaviour is currently unknown. The results displayed in Fig. 2b are in agreement with Verard's law. The lattice parameters increase as predicted by Vegard's law. The lattice parameters calculated from the most intense peak (311) are presented in Table 1 and correspond to the lattice parameter of $ZnAl_2O_4$ reported by Motloung et al. [10].

The crystallite sizes of the prepared nanocrystals were calculated using Scherrer's equation [17] and are presented in Table 1. Singly doping and co-doping slightly increased the crystallite sizes. Generally, and as expected, it is also noted that the higher (311) diffraction intensities (from Fig. 2) corresponded to bigger crystallite sizes.

3.2 Energy-dispersive X-ray spectroscopy

EDS was used to confirm the chemical composition of the host and co-doped ($x = 1.2\%$) samples as shown in Fig. 3a, b, respectively. For the host samples shown in Fig. 3a, the expected elements, namely Zn, Al and O, are observed. At concentration $x = 1.2\%$ for the co-doped sample shown in

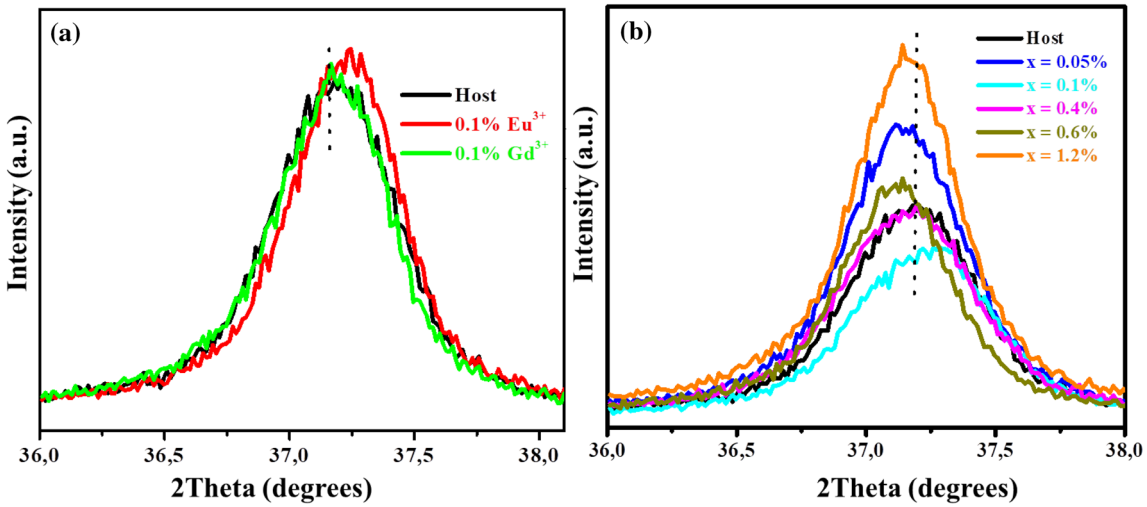

Fig. 2 Analysis of the diffraction peak corresponding to the (311) plane in the **a** host, singly doped and **b** dual-doped samples

Table 1 Sample identification of lattice parameter, crystallite size, fitting parameter, decay times and CIE colour coordinates

Sample ID	Lattice parameter (Å)	Crystallite size (nm)	Fitting parameter A	Decay time $\tau(ms)$	CIE $(x;y)$
Host	8.013	17	7099.9 ± 1.1	516.2 ± 0.1	(0.174; 0.139)
0.1% Eu^{3+}	8.003	19	5408.5 ± 0.8	515.7 ± 0.1	(0.184; 0.149)
0.1% Gd^{3+}	8.013	18	2643.0 ± 0.4	515.1 ± 0.1	(0.179; 0.156)
$x = 0.05\%$	8.020	18	6079.2 ± 0.9	515.4 ± 0.1	(0.186; 0.158)
$x = 0.1\%$	8.003	16	5418.3 ± 0.8	515.3 ± 0.1	(0.187; 0.157)
$x = 0.4\%$	8.017	16	4549.3 ± 0.7	515.0 ± 0.1	(0.197; 0.149)
$x = 0.6\%$	8.026	19	4703.6 ± 0.7	515.0 ± 0.1	(0.190; 0.160)
$x = 1.2\%$	8.020	19	3703.2 ± 0.5	514.2 ± 0.1	(0.193; 0.167)

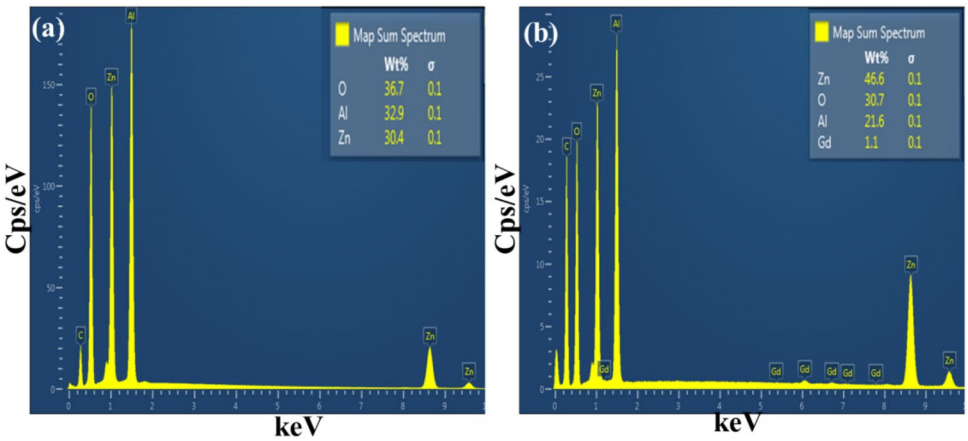

Fig. 3 The EDS spectrum of the **a** $ZnAl_2O_4$ (host) and **b** $x = 1.2\%$ nanophosphors

Fig. 3b, Gd was also observed. The element Eu was not detected in Fig. 3b, which might be due to the low concentration of Eu^{3+} ions used in this study. In all EDS spectra, the additional peak of carbon (C) is due to the sample coating. No additional impurity peaks were detected, which agrees very well with the XRD results in Fig. 1.

Figure 4 shows the EDS mapping for the $x = 1.2\%$ sample. The images of individual elements are displayed around the layered image, which suggest that the individual elements are homogeneously distributed on the surface.

3.3 Scanning electron microscopic analysis

SEM micrographs of the host, singly and co-doped samples are shown in Fig. 5. Figure 5a of the host reveals that the morphology consists of a rough surface with irregular particles of different sizes distributed all over the surface. Figure 5b of the 0.1% Eu^{3+}-doped sample shows a similar morphology, with a smaller number of irregular particles. Figure 5c shows the 0.1% Gd^{3+}-doped sample which has an intense agglomeration of particle over the surface. Figure 5d depicts the morphology of the $x = 1.2\%$ co-doped sample, which shows clusters of particles of different sizes randomly distributed. This morphology resembles both the morphologies presented in Fig. 5b, c.

3.4 High-resolution transmission electron microscopic analysis

The host, 0.1% Eu^{3+}, 0.1% Gd^{3+} and $x = 1.2\%$ samples were examined by HR-TEM to confirm the crystallite size and shape. Their respective images are presented in Fig. 6. It can be seen that the crystallites are agglomerated to each other and their average crystallite size is around 20 nm, which confirms the values predicated by the XRD as displayed in Table 1.

3.5 Photoluminescence analysis

To determine the appropriate excitation wavelength, the host sample was excited with different excitation wavelengths ranging from 260 to 310 nm. The emission spectra illustrated in Fig. 7a show that the emission peaks are located around 393 nm. The peaks at around 550, 565, 593, 605 and 631 nm are due to the second-order (2nd order) emissions corresponding to 270, 280, 290, 300 and 310, respectively. The 393 nm emission originates within the intrinsic intraband gap defects such as oxygen vacancies (V_o^*) [13, 18]. The emission intensity as a function of excitation wavelength is shown in Fig. 7b. The Gaussian fit suggests that the optimum excitation wavelength is 284 nm.

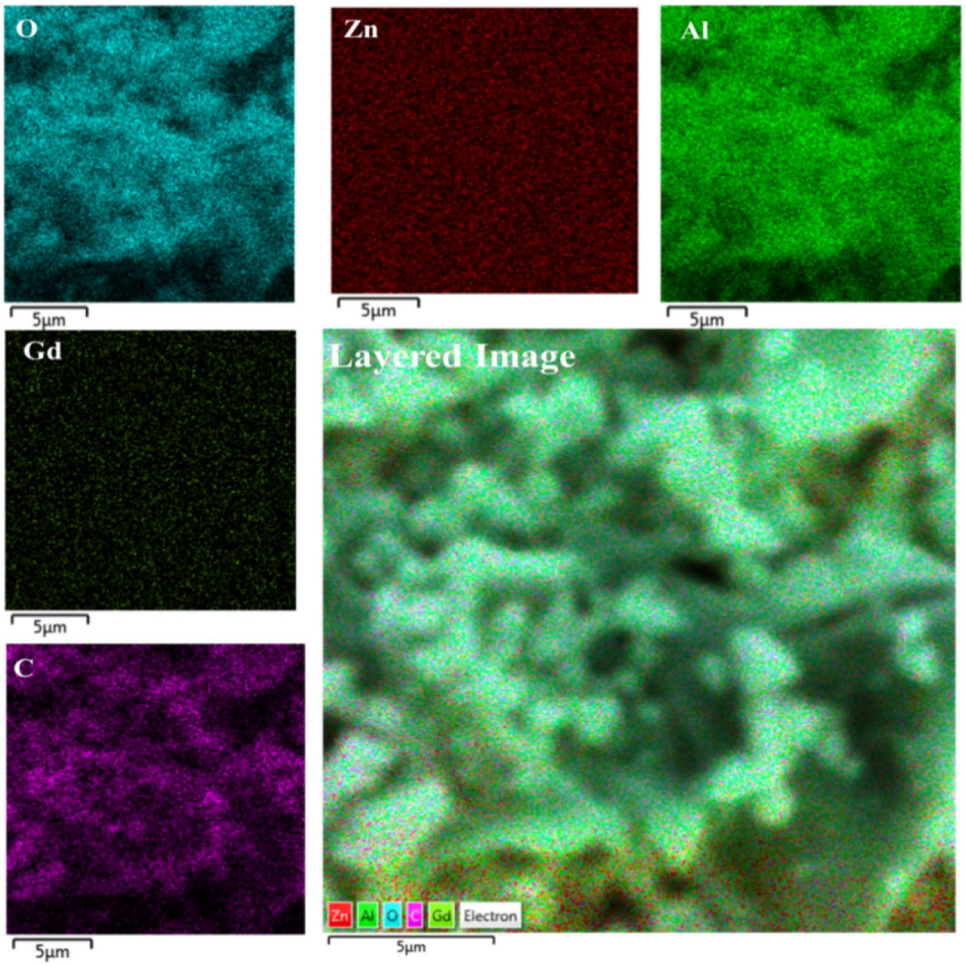

Fig. 4 EDXS elemental maps of $x = 1.2\%$ co-doped sample

The excitation and emission spectra of the host and singly doped samples are shown in Fig. 8a. The excitation spectra were taken when monitoring the violet emission at 393 nm. The excitation spectrum consists of only one band located at 284 nm (corresponds to the optimum excitation shown in Fig. 7b), which can be attributed to the band-to-band transition of AlO_6 anion grouping in $ZnAl_2O_4$ [13, 19]. Note that the emission spectra were taken when monitoring the 284 nm excitation wavelength. The emission spectrum consists of four emission peaks located at 393, 400, 578 and 618 nm. The emission at 393 and 400 nm can be attributed to the intrinsic intra-band gap since the emission at around 393–400 nm (violet) is not the characteristic of the Gd^{3+} spectroscopy [20]. The emission peak at 578 nm is a combination of the $^5D_0 \rightarrow {}^7F_1$ Eu^{3+} transition [14, 16] and the second order (2nd order) corresponding to the 284 nm excitation wavelength. The peak at 618 nm can be attributed to the $^5D_0 \rightarrow {}^7F_2$ transition within Eu^{3+} [14, 16]. To investigate the origin of each of the emission bands observed in detail, the normalized emission spectra are shown in Fig. 8b. There is no peak shift observed when the host is singly doped with 0.1% Eu^{3+}, which implies that the emission at 393 nm is from the host. However, when the host is singly doped with 0.1% Gd^{3+}, it is clear that there is a slight peak shift from 393 to 400 nm, which signifies that the trap levels responsible for the emission at 393 nm has slightly transcended downwards within the E_g [20, 21]. Figure 8c depicts the emission and excitation of the host and co-doped sample. Similar excitation and emission peaks to that of Fig. 8a are observed. Figure 8d presents the violet emission intensity at 393 nm as a function of Gd^{3+} concentration, which has been fitted by a second exponential decay behaviour. Figure 8e shows the zoomed emission region near 618 nm, and the results show that for fixed Eu^{3+} concentration (0.1%), the $x = 0.4\%$ is an optimum Gd co-dopant concentration for the Eu^{3+} $^5D_0 \rightarrow {}^7F_2$ emission. Since the Gd^{3+} ions would not be excited at 393 nm, this effect is attributed to physical changes in the nanocrystalline phosphor as a result of Gd co-doping.

The $x = 0.4\%$ co-doped sample was further excited at various wavelengths in the range of 260 to 310 nm and the emission spectra are shown in Fig. 9a. In addition to the host defect emission peak at 400 nm and Eu^{3+} peak at 618 nm discussed above, some additional second-order

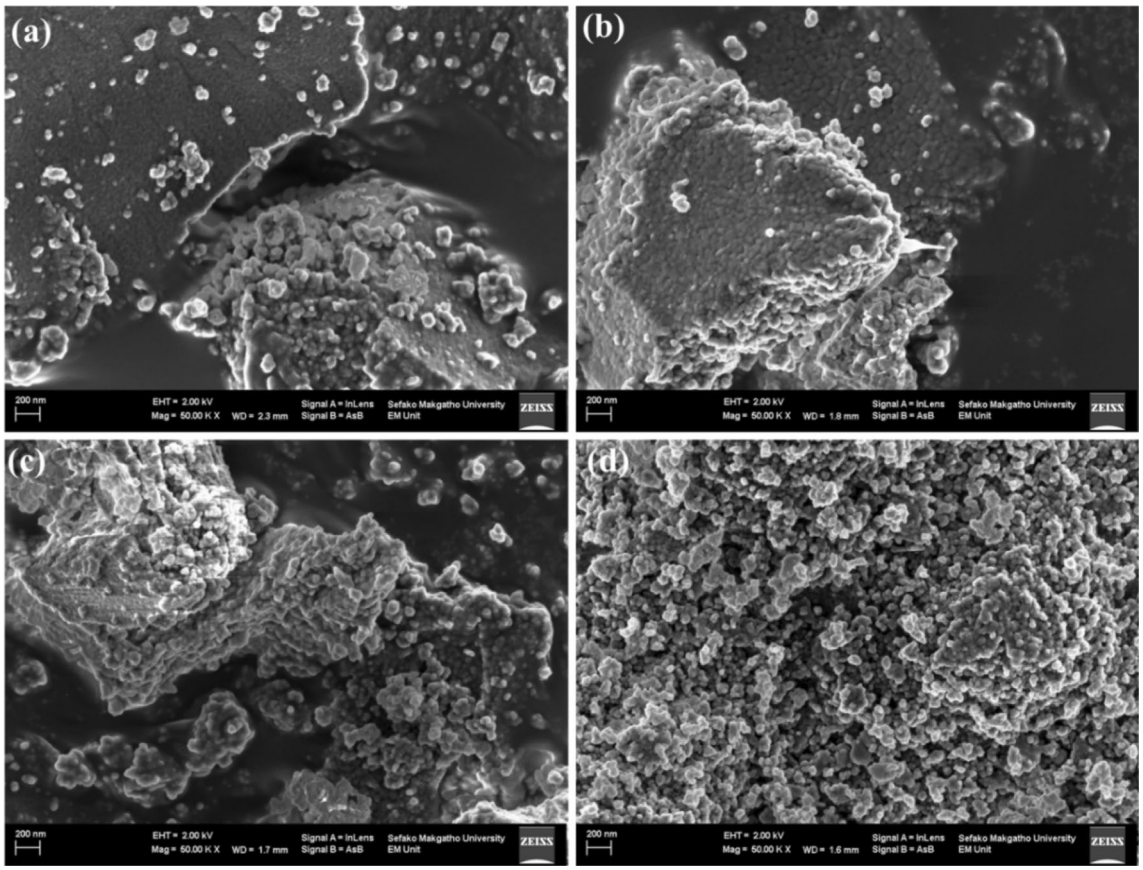

Fig. 5 The SEM micrographs of **a** host **b** singly doped with 0.1% Eu^{3+} **c** 0.1% Gd^{3+} and **d** co-doped $x = 1.2\%$ nanophoshor

peaks which shifted, corrosponding to double the excitation wavelengths, were observed. The emission intensity at 618 nm as a function of excitation wavelength is depicted in Fig. 8b. A Gaussian fit shows that to optimize the emission from Eu^{3+}, the corresponding excitation must be 263 nm. The excitation of Eu^{3+} at 263 nm is attributed to the charge transfer transition (CT) which is an electron transfer from the O^{2-} ($2p^6$) orbital from the host to the Eu^{3+} empty $4f^6$ orbital [22, 23].

The luminescence mechanisms for all emissions arising from the prepared samples are illustrated in Fig. 10. The location of the Eu^{3+} ion transitions within the host band gap was placed according to Dorenbo's diagram [24, 25]. The absence of the energy transfer from $Eu^{3+} \rightarrow Gd^{3+}$ and charge CT from the host $\rightarrow Gd^{3+}$ serves as the main reasons why there is no emission from Gd^{3+} at all. In addition and based on the Dorenbo's diagram [24-27], the results also suggest that the Gd^{3+} is located where there are no probabilities of trapping the de-excited electron within the host material. As a result, the Gd^{3+} energy levels are not shown in the emission mechanism.

3.6 Lifetime study

The radiative lifetimes of the defect emission from the prepared samples at 393 nm were measured using excitation at 284 nm. The lifetimes were fitted with the first-order exponential decay [3]:

$$I(t) = A + Be^{-t/\tau}, \quad (1)$$

where I represents the emission intensity, A is the background, B is a fitting parameter and τ is the decay time. The results are shown in Fig. 11 and the values are presented in Table 1. The lifetime of ~ 515 ms is orders of magnitude longer than that characteristic for RE emissions and indicates that carrier trapping occurs at defects in the host. Since the emission occurs on a timescale which is short compared to phosphors which are used commercially for persistent luminescence (hours), the traps are relatively shallow and detrapping occurs comparatively quickly at room temperature.

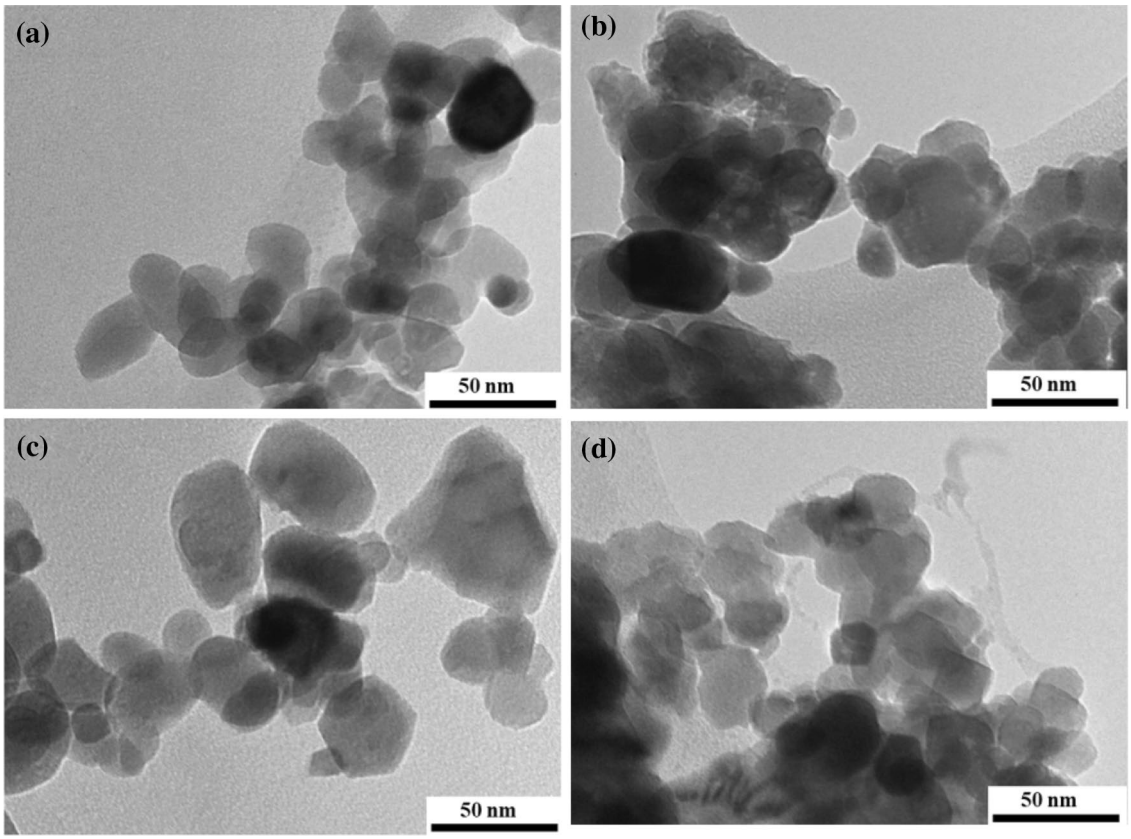

Fig. 6 HR-TEM images for the **a** host, **b** 0.1% Eu^{3+}, **c** 0.1% Gd^{3+} and **d** $x = 0.6\%$ samples

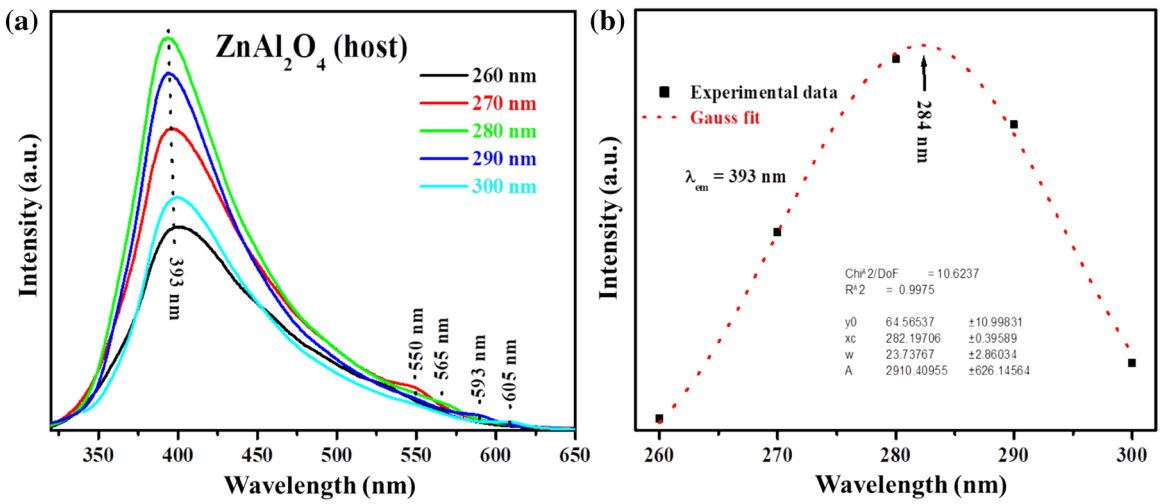

Fig. 7 **a** The emission spectra of the $ZnAl_2O_4$ (host) excited at various excitation wavelengths and **b** emission intensity as a function of excitation wavelength

3.7 Colour chromaticity

The International Commission on Illumination (CIE) colour chromaticity coordinates [28] of the prepared powders are illustrated in Fig. 12. Figure 12a illustrates the chromaticity co-ordinates of the host sample excited at different wavelengths, which falls in the violet region as expected and is not significantly changed by varying the excitation

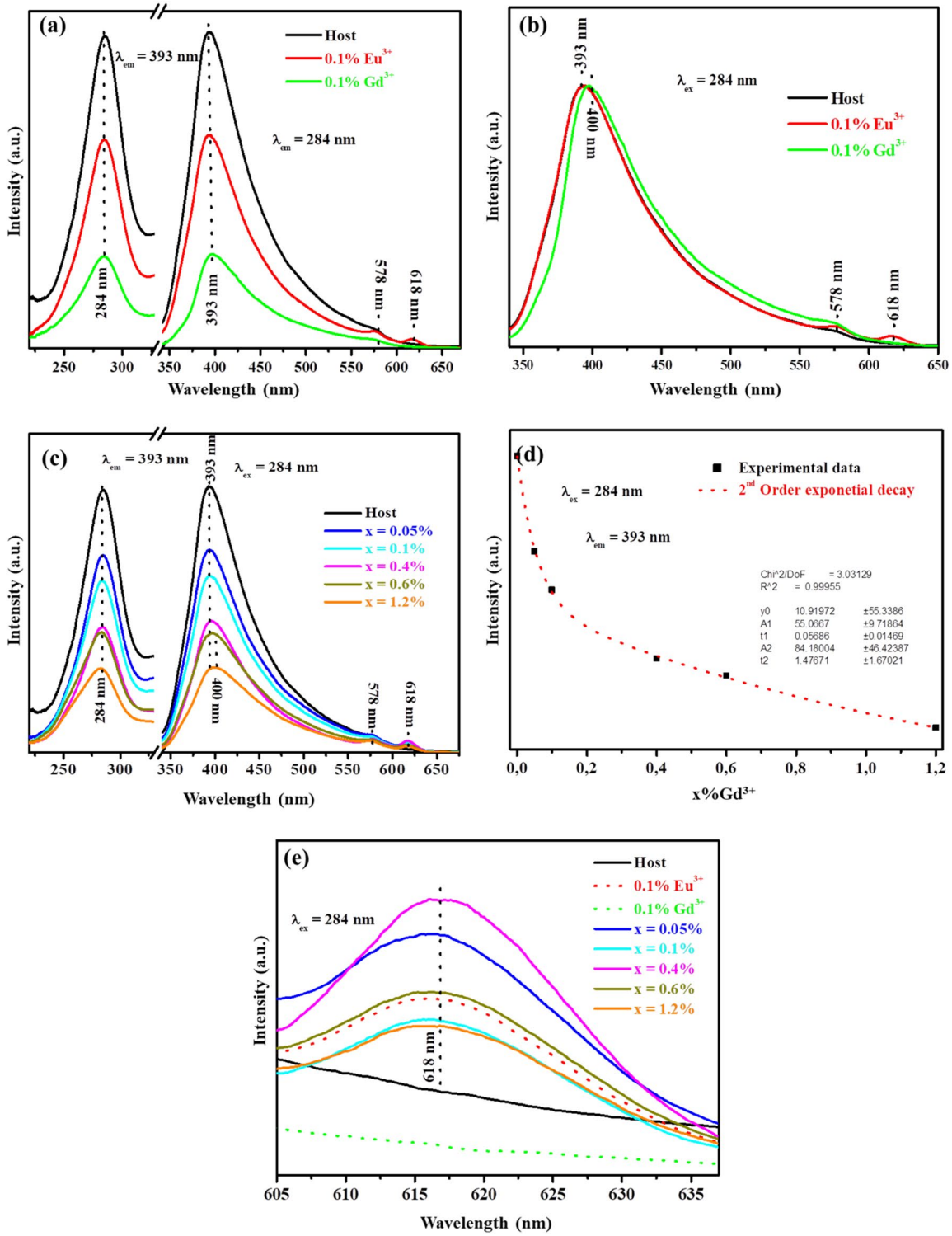

Fig. 8 Excitation and emission spectra of the **a** host and singly doped samples, **b** normalized emission for the host and singly doped samples, **c** co-doped samples at varying Gd^{3+} concentrations ($0 \leq x \leq 1.2$), **d** emission intensity of the peak located at 393 nm as a function of Gd^{3+} concentration and **e** the zoomed emission of peaks located at 618 nm

wavelength. Figure 12b illustrates the chromaticity coordinates of the host and singly doped (with 0.1% Eu^{3+} and 0.1% Gd^{3+}) excited at 284 nm. Only small shifts occur, which correspond to a slight change in the peak emission wavelength of the defect emission to ~ 400 nm when Gd is added as dopant, or a weak red emission at 618 nm when

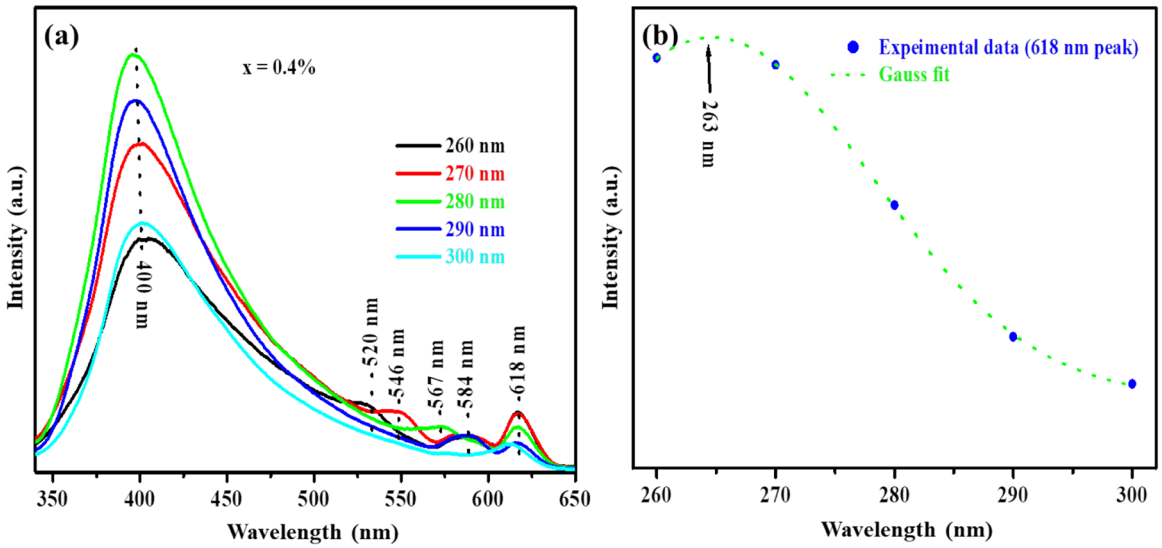

Fig. 9 **a** The emission spectra of the $x = 0.4\%$ sample excited at various excitation wavelengths and **b** emission intensity as a function of excitation wavelength

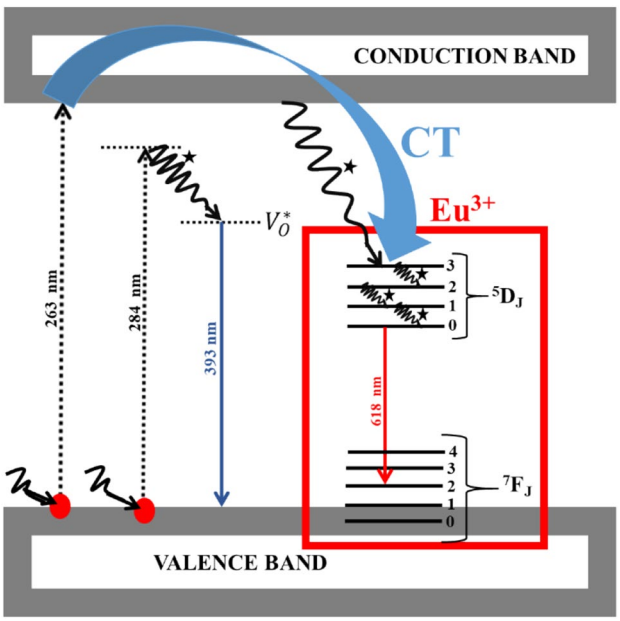

Fig. 10 The proposed excitation and emission pathway mechanism in $ZnAl_2O_4$:x% Eu^{3+}

Eu is added as dopant. This weak influence might be due to the low concentration of dopants used for the singly doped samples. However, Koao et al. [29] showed that an increase in Eu^{3+} concentration on the ZnO system shifts the emission colour towards the red emission colour. Figure 12c illustrates that the chromaticity co-ordinates for the co-doped nanophosphors and their colour coodinates are presented in Table 1. Only a small effect on the CIE colour chromaticity occurs when varying the Gd^{3+} concentration. Figure 12d shows that the emission colour from the $x = 0.4\%$ nanopowder sample shifts a little when excited at different wavelengths and moves slightly towards the centre when excited near 260–270 nm, corresponding to when the red emission from Eu^{3+} is the strongest (Fig. 9b).

4 Conclusions

A series of $ZnAl_2O_4$ nanophosphors was successfully prepared by using a citrate sol–gel technique. The undoped host and samples singly doped with either Eu or Gd (0.1%), as well as co-doped samples with 0.1%Eu^{3+} and x% Gd^{3+} ($0 \le x \le 1.2$) were studied. The XRD and HR-TEM analysis confirmed that all of the nanopowders consisted of the single-phase cubic spinel structure. EDS was able to confirm the elemental compositions of the prepared sample. SEM shows that both singly doping and co-doping influenced the host morphology. PL spectra showed an emission peak at ~ 393–400 nm, which originated from the host defects and was slightly shifted as a result of Gd doping, as well as an emission at 618 nm when Eu^{3+} ions were present. The CIE colour chromaticity showed that although slight colour shifts occur with doping and excitation wavelength, the colour in the violet region is dominated by the strong host defect emission, which has a long lifetime associated with trapping centres.

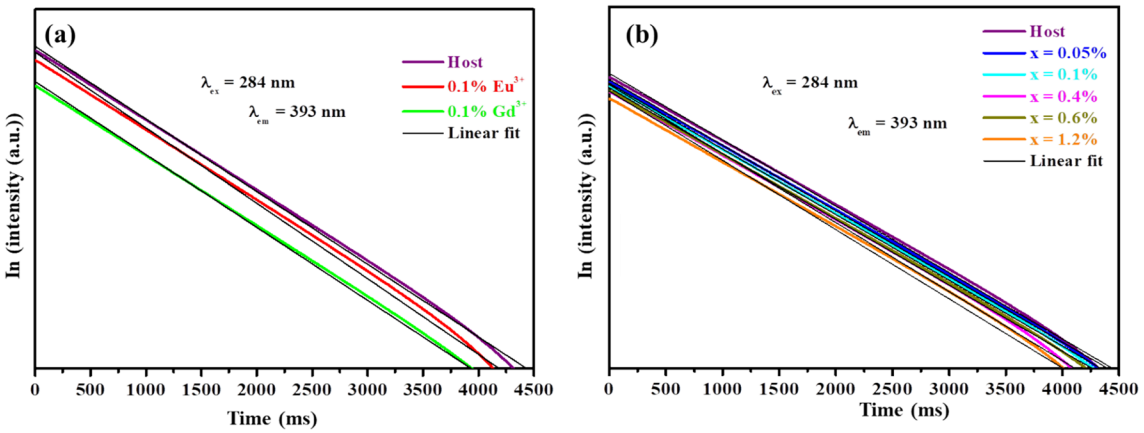

Fig. 11 Decay curves on logarithmic intensity scale of the **a** host and singly doped samples, and **b** co-doped samples

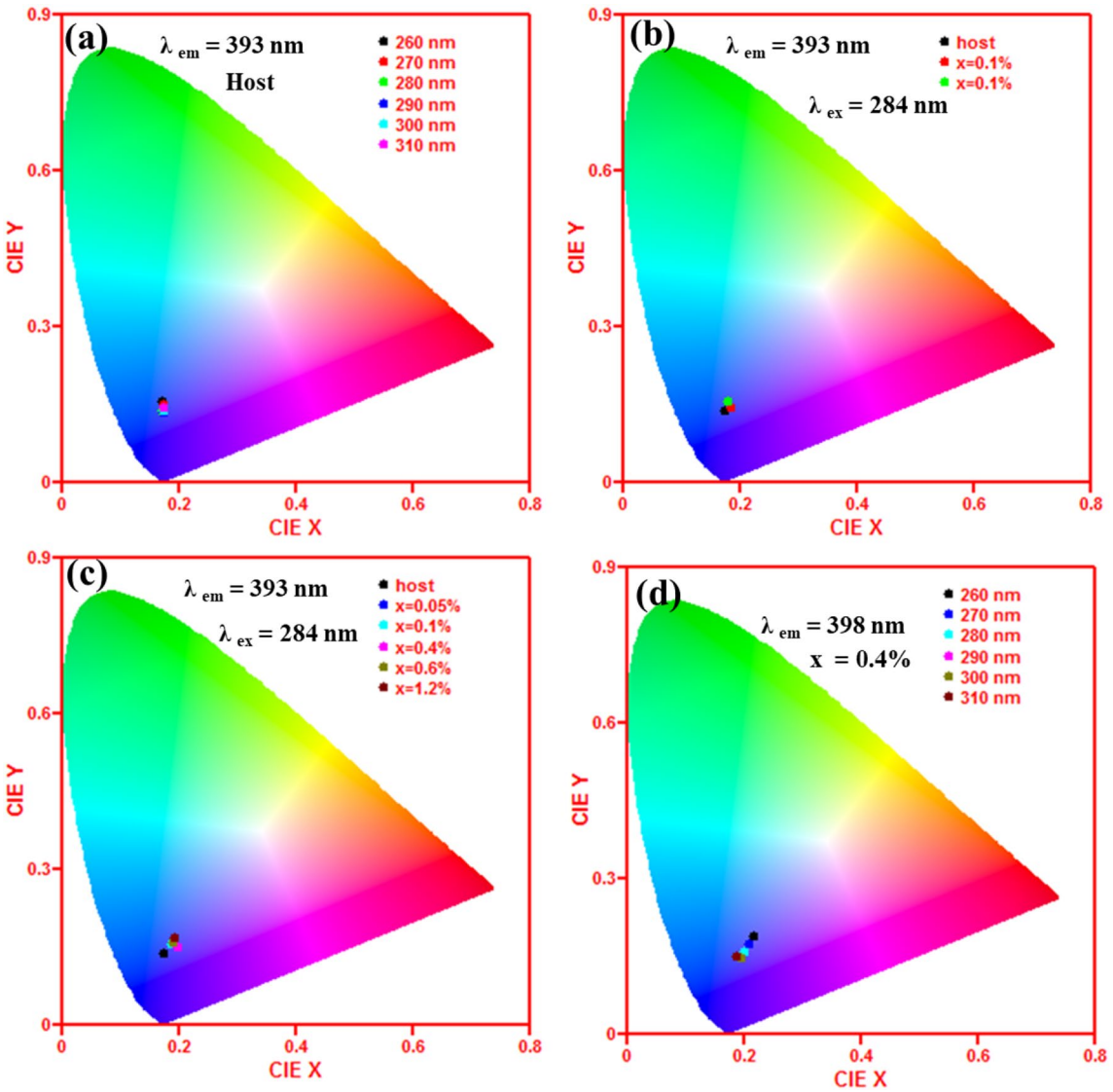

Fig. 12 CIE colour diagrams for **a** the host at varying wavelengths, **b** the host and singly doped samples excited at 284 nm, **c** co-doped samples excited at 284 nm and **d** $x = 0.4\%$ co-doped samples at varying excitation wavelengths

Acknowledgements This work was supported by the South African National Research Foundation (NRF) Thuthuka programme (Fund number: UID99266) and NRF incentive funding for rated researchers (IPRR) (Grant no: 114924). The author would also like to acknowledge Mr. T.M Manamela for the sample synthesis and Dr James Wesley-Smith at Electron Microscopy Unit at Sefako Makgatho Health Science University for the SEM and TEM imaging.

References

1. R. Roesky, J. Weiguny, H. Bestgen, U. Dingerdissen, App. Catal. A **176**, 213–220 (1999)
2. M. Zawadzki, Sol. State Sci. **8**(1), 14–18 (2006)
3. V. Singh, R.P.S. Chakradhar, J.L. Rao, D.K. Kim, J. Lumin. **128**(3), 394–402 (2008)
4. J. Popovic, B. Grzeta, B. Rakvin, E. Tkalcec, M. Vrankic, S. Kuranjica, J. Alloys Comp. **509**(34), 8487–8492 (2011)
5. G. Lakshminarayana, L. Wondraczek, J. Sol. State Chem. **184**(8), 1931–1938 (2011)
6. W.M. Mulwa, B.F. Dejene, M.O. Onani, C.N.M. Ouma, J. Lumin. **184**, 7–16 (2017)
7. W. Strek, P. Deren, A. Bednarkiewicz, M. Zawadzki, J. Wrzyszcz, J. Alloys Comp. **300–301**, 456–458 (2000)
8. D.A. Zatsepin, D.W. Boukhvalov, A.F. Zatsepin, YuA Kuznetsova, M.A. Mashkovtsev, V.N. Rychkov, V.Y. Shur, A.A. Esin, E.Z. Kurmaeva, App. Sur. Sci. **436**, 697–707 (2018)
9. R.K. Tamrakar, K. Upadhyay, Optik **143**, 125–130 (2017)
10. S.V. Motloung, F.B. Dejene, R.E. Kroon, H.C. Swart, O.M. Ntwaeaborwa, Phys B **468–469**, 11–20 (2015)
11. T. Chengaiah, C.K. Jayasankar, L.R. Moorthy, Phys B **431**, 137–141 (2013)
12. Q. Hou, F. Meng, J. Sun, Nano. Res. Lett. **8**, 144 (2013)
13. B. Cheng, S. Qu, H. Zhou, Z. Wang, Nanotechnology **17**, 2982–2987 (2006)
14. C. -Perez, J. Lambert, A. Alatorre-Ordaz, J.A. Gutierrez, T. Lopez-Luke, R. Ramirez-Fuentes, T. Kobayashi, J. Lumin. **184**, 123–129 (2017)
15. A. Nakrela, N. Benramdane, A. Bouzidi, Z. Kebbab, M. Medles, C. Mathieu, Res. Phy. **6**, 133–138 (2016)
16. S.V. Motloung, F.B. Dejene, H.C. Swart, O.M. Ntwaeaborwa, J. Sol-Gel Sci. Technol. **70**(3), 422–427 (2014)
17. V.M. Maphiri, F.B. Dejene, S.V. Motloung, Res. Phy. **7**, 3510–3521 (2017)
18. B.S. Barros, P.S. Melo, R.H.G.A. Kiminami, A.C.F.M. Costa, G.F. de Sá, S. Alves, J. Mater. Sci. **41**(15), 4744–4748 (2006)
19. H. Dixit, N. Tandon, S. Cottenier, R. Saniz, D. Lamoen, B. Partoens, V. Van Speybroeck, M. Waroquier, New J. Phy. **13**, 063002 (2011)
20. Q. Wang, S.-Y. Ouyang, W.-H. Zhang, B. Yang, Y.-P. Zhang, H.-P. Xia, Acta Metall. Sin (Engl. Lett.). **28**, 487491 (2015)
21. P. Gupta, A.K. Bedyal, V. Kumar, Y. Khajuria, S.P. Lochab, S.S. Pitale, O.M. Ntwaeaborwa, H.C. Swart, Mat. Res. Bull. **60**, 401–411 (2014)
22. W. Jiao, Z. Zhijun, Z. Jingtai, J. Rare Earths **33**(12), 1241–1245 (2015)
23. M.K. Lau, J. Hao, Energy Procedia **15**, 129–134 (2012)
24. I.A.M. Ibrahim, Z. Lences, P. Sajgalik, L. Benco, J. Lumin. **164**, 131–137 (2015)
25. Y. Shimizu, K. Ueda, J. Lumin. **168**, 14–19 (2015)
26. J.I. Eldridge, J. Lumin. **214**, 116535 (2019)
27. S.V. Motloung, K.G. Tshabalala, R.E. Kroon, T.T. Hlatshwayo, M. Mlambo, S. Mpelane, J. Mol. Struct. **1175**, 241–252 (2019)
28. hhttps://www.mathworks.com/matlabcentral/fileexchange/29620-cie-coordinate-calculatori 2012.
29. L.F. Koao, B.F. Dejene, H.C. Swart, S.V. Motloung, T.E. Motaung, Opt. Mater. **60**, 294–304 (2016)